Spin-wave confinement in a hybrid superconductor-ferrimagnet nanostructure

Julia Kharlan,[1,2] Krzysztof Sobucki,[1] Krzysztof Szulc,[1] Sara Memarzadeh,[1] and Jarosław W. Kłos[1,*]

[1] *ISQI, Faculty of Physics, Adam Mickiewicz University, Poznań, Poland*
[2] *Institute of Magnetism NASU and MESU, Kyiv, Ukraine*

(Received 21 December 2023; revised 14 March 2024; accepted 29 April 2024; published 5 June 2024)

Eddy currents in a superconductor shield the magnetic field in its interior and are responsible for the formation of a magnetic stray field outside of the superconducting structure. The stray field can be controlled by the external magnetic field and affect the magnetization dynamics in the magnetic system placed in its range. In the case of a hybrid system consisting of a superconducting strip placed over a magnetic layer, we theoretically predict the confinement of spin waves in the well of the static stray field. The number of bound states and their frequencies can be controlled by an external magnetic field. We present the results of semianalytical calculations complemented by numerical modeling.

DOI: 10.1103/PhysRevApplied.21.064007

I. INTRODUCTION

The states of superconductivity and ferromagnetism are very rarely observed in a single material. Their intrinsic coexistence (i.e., in one uniform phase for the same electrons) was found for triplet pairing in a proximity to a magnetic quantum critical point (e.g., for UGe_2) [1,2]. The other possibility, known for a long time and more conventional [3,4], is the coexistence of two phases where large and localized moments of 4f electrons (Er, Gd) provide long-range strong ferromagnetism whereas 3d conduction electrons are responsible for superconductivity.

The hybrid systems [5–8], where the superconductor and ferromagnet are part of the same structure and interact with each other, usually offer much more flexibility both in the design and implementation of new features. Superconductor-ferromagnet hybrids can be divided into two categories: both subsystems are in direct contact [9] or separated by a nonmagnetic, nonconducting material. In the latter case, the coupling at a distance results from the fact that both the eddy currents in the superconductor and the magnetic moments in the ferromagnet generate a magnetic field. The coupling provided by the magnetic field can be controlled by the external magnetic field and can be tailored by the geometry, since both the distribution of the eddy currents and the magnetization configuration depend on these factors.

In electromagnetically coupled hybrids, the ferromagnet can modify the properties of the superconductor, e.g., the magnetic screening can increase the value of the critical current density in the superconductor [10], or the presence of the stray field produced by ferromagnetic nanoelements can affect the nucleation of vortices [11] or pin and guide the vortices in the superconductor [12]. Similarly, the presence of the superconductor can influence the ferromagnet, e.g., by controlling the magnetization dynamics [13,14]. In this research field, we can find reports about induction of magnonic crystals and nonreciprocal spin-wave (SW) transmission in uniform magnetic layers due to the screening of the dynamic demagnetizing field by a superconductor [15,16], magnon-phonon interaction [17,18], the gating of magnons induced by a superconducting current [19,20], enhancement of nonlinear SW dynamics [21], Bragg scattering of SWs on the field produced by the Abrikosov vortex lattice [22,23], or SW generation by moving vortices [24–26]. Undoubtedly, superconductor-ferromagnet hybrids offer many possibilities for controlling the dynamics of SWs. One of the topics not fully explored is the problem of localization of SWs in these systems.

In this study, we conduct a theoretical and numerical investigation of the SW confinement induced in a uniform ferrimagnetic (FM) layer by the stray field of a superconducting (SC) strip. We demonstrate that by adjusting the applied field, we can control the depth of the stray field to modify the number of confined SW modes and their frequencies.

II. MODEL

The considered hybrid system consists of an FM gallium-doped yttrium iron garnet (Ga:YIG) thin film and an SC Nb strip in the Meissner state, electrically isolated from each other by a thin nonmagnetic spacer (see Fig. 1). According to the Meissner effect, an SC strip expels a

*Corresponding author: klos@amu.edu.pl

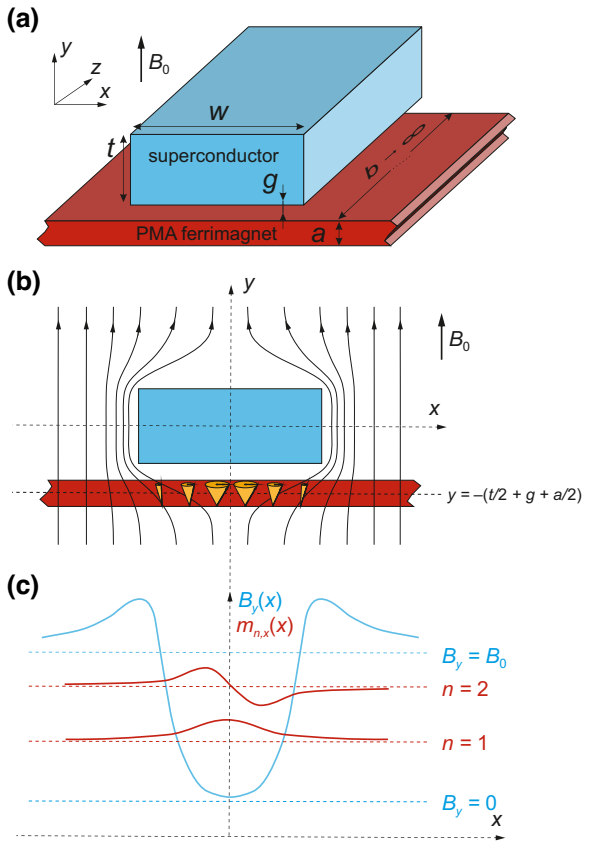

FIG. 1. (a) A thin FM film ($a = 20$ nm) is exposed to the stray field of a rectangular SC strip ($w = 400$ nm, $t = 100$ nm). The ferrimagnet (Ga:YIG) and the superconductor (Nb) are separated by a small gap ($g = 10$ nm). The magnetic film has low M_s and exhibits PMA, so it is magnetized out of plane in the absence of the external magnetic field. Sketches (b) and (c) illustrate the mechanism of SW localization. (b) The internal static magnetic field is lowered in the region of the ferrimagnet underneath the SC strip. This leads to the confinement of SW modes (c), which are quantized in the quasiparabolic well of the internal field.

magnetic field from its volume by means of eddy currents. These currents create a nonuniform distribution of the magnetic field throughout the entire space, including the FM film. Such a geometry enables the investigation of the coupling between FM and SC subsystems as purely classical, where the stray magnetic field from the eddy currents in the SC strip impacts the magnetization in the FM layer.

The system is placed in an external magnetic field perpendicular to the FM layer. In Ga:YIG, the shape anisotropy is overcome by the perpendicular magnetic anisotropy (PMA), leading to the magnetization being directed out of plane even in the absence of an external magnetic field. Operating with the relatively small external field, we can sustain the Meissner state in a confined geometry of the strip, and observe the impact of the stray field of the SC strip on the magnetization dynamics in the FM layer. Then, the stray field of the SC strip is tuned by the external field and induces the well of the static effective field of controllable depth in the FM layer. The well can confine the SWs of frequencies lower than the ferromagnetic resonance (FMR) frequency of the FM layer in the absence of an SC strip.

Any static stray field is not produced outside a uniformly magnetized infinite FM layer—only the internal demagnetizing field ($-M_s\hat{\mathbf{y}}$) is present. However, the stray field of the SC strip induces a weak magnetization texture in the FM layer, close to the SC-strip edges. It can produce a static stray field, although it is small and can be neglected; see Appendix A. The dynamic stray field coming from the SW modes in the FM layer can also be considered negligible. For the FM layer magnetized in the out-of-plane direction, the dynamic components of magnetization are tangential to the surfaces and do not produce any surface magnetic charges. On the other hand, the dynamic stray field can be generated by the volume magnetic charges, but it requires a strong nonuniformity of the SW profile, which is observed for the higher SW modes (not investigated here). Therefore, we assume that eddy currents are unaffected by SWs and remain constant. To sum up, both static and dynamic stray fields induced in the FM layer are negligible for the SC strip. Therefore, there is no need to solve the self-consistent problem for our system and take into account the mutual interaction between the FM layer and the SC strip. For the considered magnetization configuration in the FM layer (i.e., out-of-plane saturation), the system is in the forward volume geometry, so any change in the dynamic stray field resulting from the presence of the SC strip will not induce the nonreciprocity effect observed in superconductor-ferromagnet hybrids [16]. Therefore, the time-reversal symmetry remains unbroken and the confined SWs have the form of standing modes.

Taking these assumptions into account, our studies were carried out in two stages. We first calculated the static stray field generated by the SC strip. It was determined from the distribution of SC currents, which was found by a semianalytical solution of the London equations. The static field generated by the SC strip was then included as a correction to the effective field in the Landau-Lifshitz (LL) equation. The LL equation was solved both semianalytically and numerically and was used to find the confined SW modes.

A. Static magnetic field produced by a superconducting strip

The London equation has been solved analytically for a number of geometries, such as a film [27], a cylindrical wire [28], and an infinitely thin cylindrical dot [29]. However, the analytical solution of the London equation presents difficulties, even for such a simple structure as a

strip, due to the impossibility of variable separation. We have therefore used the semianalytical method developed by Brandt [30,31]. For the SC strip in an external field applied along the y direction $\mathbf{B}_0 = B_0\hat{\mathbf{y}}$, the Meissner effect induces a current of density $\mathbf{J} = J(x,y)\hat{\mathbf{z}}$ flowing along the z axis and generating a stray field $\mathbf{B}_{sc}(x,y)$, which lacks a z component; see Fig. 1(b). According to Ampère's law, we can relate the current density to the total field $\mathbf{B}$ and vector potential $\mathbf{A}$ as

$$\mu_0\mathbf{J} = \nabla\times\mathbf{B} = \nabla\times\nabla\times\mathbf{A} = -\Delta\mathbf{A}, \tag{1}$$

where we have used the Coulomb gauge ($\nabla\cdot\mathbf{A} = 0$), and μ_0 denotes the permeability of vacuum. Equation (1) can be interpreted as a two-dimensional Poisson equation for vector potential $\mathbf{A} = A(x,y)\hat{\mathbf{z}}$ with a current $\mathbf{J} = J(x,y)\hat{\mathbf{z}}$ being a source:

$$\Delta A(x,y) = -\mu_0 J(x,y) \tag{2}$$

where Δ is a two-dimensional Laplacian. Let us decompose the vector potential $\mathbf{A} = [xB_0 + A_{sc}(x,y)]\hat{\mathbf{z}}$ into the contribution related to the uniform external field, $\mu_0 xH_0$, and the field produced by the SC, $A_{sc}(x,y)$, and then relate the latter inside the SC to a current $J(x,y)$ using the London equation with Coulomb gauge:

$$A_{sc}(x,y) = -\mu_0\lambda^2 J(x,y) \tag{3}$$

with λ the London penetration depth. Then, using Eq. (3), we can write Eq. (2) in the integral form

$$\lambda^2 J(x,y) = \iint_S dx'\,dy' Q(x,y,x',y')J(x',y') + xH_0, \tag{4}$$

where S is the cross section of the SC strip in x-y plane and the function $Q = \ln[\sqrt{(x-x')^2+(y-y')^2}]/2\pi$ is the integral kernel for the two-dimensional Laplace operator.

Equation (4) can be integrated numerically by sampling the function $J(x,y)$ on a square grid of equidistant points (x_i,y_j): $x_i = [(i-\frac{1}{2})/N_x - \frac{1}{2}]w$, $y_j = [(j-\frac{1}{2})/N_y - \frac{1}{2}]t$, $i = 1,\ldots,N_x$, $j = 1,\ldots,N_y$. Here w and t are the strip width and thickness, respectively (see Fig. 1), and N_x and N_y are number of points in the x and y directions, where $N_x/w \approx N_y/t$. By marking the points $\mathbf{r}_l = (x_i,y_j)$ with an index $l = 1,\ldots,N = N_xN_y$, the function $J(x,y)$ becomes a vector J_l with N components, and the integral kernel is transformed into the $N\times N$ matrix $Q_{l,l'}$. Note that $Q_{l,l'}$ diverges for $l = l'$, which should be avoided. Equation (4) for the distribution of the current density $J(x,y)$ can then be rewritten in matrix form:

$$\lambda^2 J_l = \sum_{l'}\tilde{Q}_{l,l'}J_{l'} + \frac{1}{\mu_0}x_{l'}B_0 \tag{5}$$

with $\tilde{Q}_{l,l'} = Q_{l,l'}(w/N_x)(t/N_y)$. The solution of Eq. (5) for J_l can be found when we invert the matrix $P_{l,l'} = \lambda^2\delta_{l,l'} - \tilde{Q}_{l,l'}$:

$$J_l = \frac{1}{\mu_0}B_0\sum_{l'}(P^{-1})_{l,l'}x_{l'}. \tag{6}$$

Finally, the distribution of field B_{sc} produced by eddy currents can be determined using the Biot-Savart law:

$$B_{sc,x}(x,y) = \frac{\mu_0}{2\pi}\iint_S dx'\,dy'\frac{J(x',y')(y'-y)}{(x'-x)^2+(y'-y)^2}, \tag{7a}$$

$$B_{sc,y}(x,y) = -\frac{\mu_0}{2\pi}\iint_S dx'\,dy'\frac{J(x',y')(x'-x)}{(x'-x)^2+(y'-y)^2}. \tag{7b}$$

The integrals in Eqs. (7) can be calculated numerically by sampling the current density J on the cross section S of the SC strip.

B. Spin-wave modes confined in the well of the magnetic field induced by a superconducting strip

After calculating the stray field generated by the SC strip, the next step is to investigate the SW localization in the FM layer placed under the strip. Two assumptions were made in our theoretical model: (i) our calculations have shown that the magnetic field generated by the SC strip does not vary significantly across the thin FM layer, so we assume that the SC field does not depend on the y coordinate and is equal to the value at the film center; (ii) we have neglected the tangential component of the SC field and, consequently, the deviation of the magnetization from the film normal, so we have included only the normal component of the SC field, which is responsible for the formation of the well for localized SW modes, and thus considered the uniform magnetization directed perpendicular to the film plane.

The magnetization dynamics in the continuous medium is described semiclassically by the LL equation:

$$\frac{\partial\mathbf{M}(\mathbf{r},t)}{\partial t} = -|\gamma|\mu_0\mathbf{M}(\mathbf{r},t)\times\mathbf{H}_{eff}(\mathbf{r},t). \tag{8}$$

Here γ is the gyromagnetic ratio and $\mathbf{H}_{eff}$ is the effective magnetic field, calculated from the free energy density [32]

$$F = -(\mathbf{B}_0+\mathbf{B}_{sc})\cdot\mathbf{M} + \frac{A_{ex}}{M_s^2}(\nabla\mathbf{M})^2 - \frac{1}{2}\mu_0\mathbf{H}_d\cdot\mathbf{M} - \frac{K_u}{M_s^2}(\mathbf{M}\cdot\hat{\mathbf{n}})^2 \tag{9}$$

with respect to magnetization:

$$\mathbf{H}_{eff} = -\frac{1}{\mu_0}\frac{\delta F}{\delta\mathbf{M}}.$$

Also, in Eq. (8), we neglected damping. The material parameters in Eq. (9), M_s, A_{ex}, and K_u, denote the saturation magnetization, exchange-stiffness constant, and uniaxial anisotropy, respectively. In our case, the magnetocrystalline anisotropy is easy-axis anisotropy ($K_u > 0$), oriented in the out-of-plane direction ($\hat{\mathbf{n}} = \hat{\mathbf{y}}$) that overcomes the shape anisotropy ($K_u > \mu_0 M_s^2/2$). The demagnetizing field is nonlocal [which means that $\mathbf{H}_d(\mathbf{r}, t)$ at specific point $\mathbf{r}$ depends on the magnetization distribution in the whole magnetic body]. We use the linear approximation, where the magnetization precesses harmonically around the equilibrium position $\mathbf{M}_0(\mathbf{r}) = M_s\hat{\mathbf{y}}$ with amplitude $\mathbf{m}(\mathbf{r}) = m_x\hat{\mathbf{x}} + m_z\hat{\mathbf{z}}$ much smaller than the static magnetization component [$|\mathbf{m}(\mathbf{r})| \ll M_s$], giving the total magnetization vector $\mathbf{M}(\mathbf{r}, t) \approx \mathbf{M}_0(\mathbf{r}) + \mathbf{m}(\mathbf{r})e^{i\omega t}$. Then, we can decompose the demagnetizing field into a static and dynamic component $\mathbf{H}_d(\mathbf{r}, t) \approx -M_s\hat{\mathbf{y}} + \mathbf{h}_d(\mathbf{r})e^{i\omega t}$, where the dynamic component $\mathbf{h}_d = h_{d,x}\hat{\mathbf{x}} + h_{d,z}\hat{\mathbf{z}}$ can be written in general form:

$$\mathbf{h}_d(\mathbf{r}) = -\nabla \int_V dv' \mathbf{m}(\mathbf{r}') \cdot \nabla' \frac{1}{4\pi|\mathbf{r} - \mathbf{r}'|}. \tag{10}$$

The LL equation (8) can then be written in linearized form:

$$i\omega m_x(x) = |\gamma|\left[\left(B_0 - \mu_0 M_s + \frac{2K_u}{M_s} + B_{sc,y}(x)\right)m_z(x) - \frac{2A_{ex}}{M_s}\frac{d^2}{dx^2}m_z(x) - \mu_0 M_s h_{d,z}(x)\right], \tag{11a}$$

$$-i\omega m_z(x) = |\gamma|\left[\left(B_0 - \mu_0 M_s + \frac{2K_u}{M_s} + B_{sc,y}(x)\right)m_x(x) - \frac{2A_{ex}}{M_s}\frac{d^2}{dx^2}m_x(x) - \mu_0 M_s h_{d,x}(x)\right]. \tag{11b}$$

Here we have used the assumption that inside the thin FM layer both the magnetization and field are constant in an out-of-plane direction, i.e., they do not depend on the y coordinate, and the tangential component of the stray field of the SC can be neglected: $B_{sc,x} \approx 0$.

In most cases, it is impossible to obtain a rigorous analytical solution of the LL equation for SWs in nanostructures. Usually, the eigenfunctions of the exchange-field operator, which, however, are not eigenfunctions of the operator for the demagnetizing field, are used as trial functions in the Ritz method. Such an approach, when applied to planar nanoelements with relatively uniform magnetization distribution, allows one to obtain solutions that are close to the exact ones [33–36]. In these systems, the demagnetizing field is almost constant in the whole volume (due to the small magnetic volume charges), except in the vicinity of the edges (where surface magnetic charges play a role). However, such an approach does not work in the case of nanoelements with strongly inhomogeneous demagnetizing or external fields. In such cases, it is necessary to consider trial solutions being the eigenfunctions of the operator, which is a sum of the exchange operator and the operators that express the impact of demagnetizing effects or external fields. For instance, the SW localization in a tangentially magnetized thin layer induced by the dipolar stray field of the magnetic sphere was considered in Ref. [37]. In this system, the static stray field of the sphere, perceptible by the SW in the FM layer, was approximated by parabolic functions. In the framework of this approximation, the linearized LL equation was reduced to a system of coupled Schrödinger-like equations for a quantum harmonic oscillator with the dynamic demagnetizing field of the FM layer considered as a perturbation [37–39]. Therefore, the eigenfunctions in the form of Hermite polynomials could be chosen as trial solutions for SW modes.

Considering the assumptions made at the beginning of Sec. II, we can use the approach proposed in Ref. [37] for investigating superconductor-ferrimagnet hybrid systems. The linearized LL equation can then be written in compact form:

$$i\omega m_x(x) = |\gamma|[\Xi(x)m_z(x) - \mu_0 M_s h_{d,z}(x)], \tag{12a}$$

$$-i\omega m_z(x) = |\gamma|[\Xi(x)m_x(x) - \mu_0 M_s h_{d,x}(x)]. \tag{12b}$$

The operator

$$\Xi(x) = -\frac{2A_{ex}}{M_s}\frac{d^2}{dx^2} + B_y(x)$$

describes the impact of the dynamic exchange field and the total static field,

$$B_y(x) = B_0 - \mu_0 M_s + \frac{2K_u}{M_s} + \underbrace{B_0[\beta_0 + \beta_2 x^2 + O(x^2)]}_{B_{sc,y}(x)}, \tag{13}$$

on magnetization dynamics. It is worth noting that, according to Eqs. (6) and (7), the stray field $B_{sc,y}(x)$ is linearly scaled by the external field B_0.

By introducing circular polarization for the dynamic component of magnetization, $m = m_z + im_x$, and neglecting the dynamic demagnetizing field $\mathbf{h}_d$, we can transform the set of equations (12) into a form equivalent to the stationary Schrödinger equation:

$$\Xi(x)\, m_n(x) = \frac{1}{|\gamma|}\omega_{0,n} m_n(x). \tag{14}$$

Equation (14) can be solved analytically after neglecting higher-order terms in the expansion in Eq. (13). The problem is then reduced to the magnonic counterpart

of the quantum harmonic oscillator with equidistant eigenfrequencies $\omega_{0,n}$ and corresponding eigenfunctions $m_n(x)$ expressed by Hermite polynomials $H_n(\xi) = (-1)^n \exp(\xi^2)\, d^n \exp(-\xi^2)/d\xi^n$:

$$m_n(\xi = Kx) = CM_s \underbrace{\frac{1}{\sqrt{2^n n!\sqrt{\pi}}} \exp(-\xi^2) H_n(\xi)}_{\psi_n(\xi)} \quad (15)$$

for every nth SW mode. The scaling factor $K = \sqrt[4]{B_0\beta_2 M_s/2A_{ex}}$ expresses the interplay between the strength of the exchange interaction and the curvature (strength) of the well of the SC stray field, in which the SW modes are confined. The real function $\psi_n(\xi)$ is normalized, $\int_{-\infty}^{\infty} \psi_n(\xi) = 1$, and the dimensionless constant C expresses the complex SW amplitude.

The approximation $B_{sc,y}(x) \approx B_0(\beta_0 + \beta_2 x^2)$ is not valid for wide SC strips, $w \gg \lambda$ [where the well $B_{sc,y}(x)$ becomes relatively flat at the bottom], and narrow strips, $w < \lambda$, or small B_0 (where the well is shallow and distortion of its parabolic shape, related to the presence of the barriers on its sides, affects the mode of the lowest frequency). Therefore, we solve Eq. (14) numerically for the stray field $B_{sc,y}$ in its full form given by Eqs. (7)—this task is relatively simple and does not demand extensive computations. The obtained frequencies $\tilde{\omega}_{0,n} \neq \omega_{0,n}$ of the bound SW modes were calculated for a realistic (i.e., nonparabolic) stray field of the SC strip, but with dynamic dipolar interaction neglected. However, we used the approximated (by Hermite polynomials) profiles of the eigenmodes from Eq. (15) to include the role of dynamic dipolar interactions.

The next step in our computational procedure is to include the impact of the dynamic demagnetizing field $\mathbf{h}_d$ and correct the frequencies of individual modes $\tilde{\omega}_{0,n}$ calculated in the absence of $\mathbf{h}_d$. We are going to limit our calculations to the so-called diagonal approximation [39], which was satisfactory for many similar cases [37,38], where the difference between successive frequencies $\tilde{\omega}_{0,n}$ is large with respect to the frequency shift due to the dynamic dipolar interaction. This approximation also neglects the intermode dipolar coupling. According to Eq. (10), the dynamic demagnetizing field produced by a single mode can be written in the form

$$h_{d,p,n}(x) = -\int_V dv' \sum_q m_{q,n}(x') \frac{d^2}{dp\, dq'} \frac{1}{4\pi|\mathbf{r} - \mathbf{r}'|}, \quad (16)$$

where the indices p and q run over the coordinates x and z, and the derivative d/dq' means d/dx' (or d/dz') for $q = x$ (or $q = z$). We denote by $m_{q,n}(x)$ the components of dynamic magnetization for the nth mode.

The spectrum of eigenmodes, which includes the correction resulting from the presence of the dynamic dipolar interaction, has the form (see Appendix B for a derivation)

$$\omega_n = \sqrt{(\tilde{\omega}_{0,n} - |\gamma|\mu_0 M_s \langle\tilde{h}_{d,x}\rangle_n)(\tilde{\omega}_{0,n} - |\gamma|\mu_0 M_s \langle\tilde{h}_{d,z}\rangle_n)}, \quad (17)$$

where the $\langle\tilde{h}_{d,p}\rangle_n$ are averaged and normalized (dimensionless) components of $\mathbf{h}_d$. The averaged field $\langle\tilde{h}_{d,z}\rangle_n$ is equal to zero in the considered system, whereas $\langle\tilde{h}_{d,x}\rangle_n$ can be expressed by the compact formula (see Ref. [37] and Appendix C)

$$\langle\tilde{h}_{d,x}\rangle_n \approx -\frac{1}{K}\int_{-\infty}^{\infty} dk_x \left(1 - \frac{1 - e^{-k_x a}}{k_x a}\right) \tilde{\psi}_n\left(\frac{k_x}{K}\right), \quad (18)$$

where $\tilde{\psi}_n(\mathcal{K}) = (1/\sqrt{2\pi}) \int_{-\infty}^{\infty} e^{-i\mathcal{K}\xi} \psi_n(\xi) d\xi$ is the Fourier transform of $\psi(\xi)$. The one-dimensional integral in Eq. (18) is relatively simple to compute compared to the calculations of $\langle\tilde{h}_{d,u}\rangle_n$ directly from Eq. (16). It is worth noting that we approximate $m_{p,n}(x)$ by taking $m_{p,n}(x) \approx C_p M_s \psi_n(Kx)$, where the $\psi_n(Kx)$ are eigenfunctions of $\Xi(x)$. The amplitudes C_p are canceled during normalization; see Appendix C.

1. Micromagnetic simulations

To perform micromagnetic simulations, we used the open-source environment MUMAX^3 [40] that solves the LL equation using the finite-difference method in the time domain. We discretized the system with a regular mesh with unit cell $2 \times 20 \times 20$ nm^3 (along the x, y, and z axes, respectively). The system was placed in an inhomogeneous external magnetic field $\mathbf{B}_0 + \mathbf{B}_{sc}(\mathbf{r})$ that includes the full contribution of the stray field of the SC strip. The field profile was imported from an external file containing the results of semianalytic calculations of $\mathbf{B}_{sc}(\mathbf{r})$. We applied the periodic boundary conditions along the z axis (1024 repetitions) to simulate an infinitely long strip. We increased the damping constant close to the edges of the domain perpendicular to x axis from $\alpha_{edge} = 0$ to 0.5 in order to eliminate the reflections along x-axis edges. The SWs in the system were numerically excited by a rectangular model antenna of width 12 nm, placed in the center of the film. The antenna generated a local dynamic magnetic field described by the function $H_{ant}(t) = H_0\, \mathrm{sinc}[2\pi f_{cut}(t - t_0)]\hat{x}$, where $\mu_0 H_0 = 0.024 B_0$ and f_{cut} is a cutoff frequency that varies in the simulations depending on the depth of the well of the stray field $\Delta B_{sc,y}$; see Fig. 2(a). For each $\Delta B_{sc,y}$, the simulation was run for a time span of $1000/f_{cut}$. The results of the simulations were saved continuously as snapshots of the magnetic configuration with time sampling $t_{sample} = 0.5/(1.5 f_{cut})$. In the postprocessing, all saved magnetic configurations were used to calculate the spectra by employing the Fourier transform. The visualizations of particular modes in the system

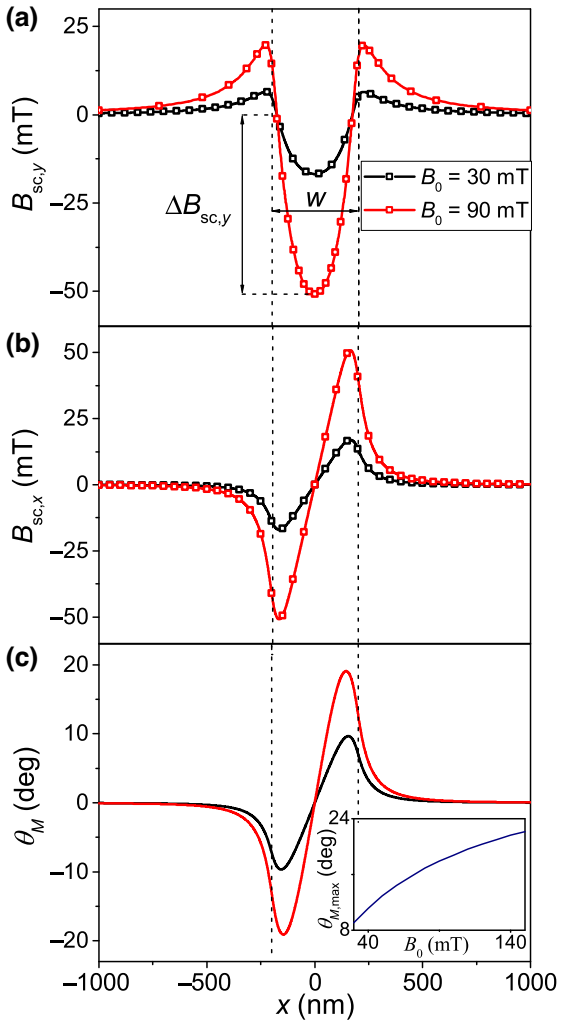

FIG. 2. The profiles of the magnetic field components (a) $B_{sc,y}$ and (b) $B_{sc,x}$ produced by the SC strip, calculated using Eqs. (7) (solid lines) and using numerical simulations (open squares). (c) The deflection θ_M of the magnetization from the direction of the external field $\mathbf{B}_0 = B_0\hat{\mathbf{y}}$. The inset plot shows the evolution of the maximum angle deviation with the external magnetic field value. Profiles (a)–(c) are plotted along the line $y = -70$ nm, passing through the center of the film. Dashed vertical lines mark the edges of the SC strip. Black and red lines correspond to the external field B_0 equal to 30 and 90 mT, respectively. Note that, to calculate the total magnetic field, we have to sum $\mathbf{B}_0$ and $\mathbf{B}_{sc}$.

were done by calculating the inverse Fourier transform of frequencies corresponding to the modes.

Micromagnetic simulations were also used to calculate the stray field produced by magnetization texture in the FM layer resulting from the action of a stray field from the SC strip; see Appendix A.

2. Finite-element method

Numerical simulations were performed in COMSOL Multiphysics® using the finite-element method (FEM) in order to calculate the stray field coming from the SC strip subjected to the external magnetic field. To be consistent with the semianalytical calculations, we used the London equation

$$\Delta A = \frac{1}{\lambda^2} A \tag{19}$$

inside the SC material and Ampère's law

$$\Delta A = 0 \tag{20}$$

outside of the SC material, both modified to the form for magnetic vector potential A. We investigated the system in the two-dimensional model in the x-y plane. In this case, the Coulomb gauge $\nabla \cdot \mathbf{A} = 0$ and the condition on the SC boundary $\mathbf{A} \cdot \mathbf{n} = 0$ are automatically fulfilled. The external magnetic field B_0 was applied as a boundary condition $-\partial_x A = B_0$ far away from the SC material. Here, the SC strip was placed in the center of a 100-μm square-shaped cell, on which boundary this condition is applied.

We checked the validity of the London model for the considered SC structure by the FEM calculation of the stray field based on the Ginzburg-Landau model; see Appendix D.

III. RESULTS

We considered an SC strip of thickness $t = 100$ nm and width $w = 400$ nm (or 800 nm for comparison). The strip was made of Nb, for which we took the London penetration depth $\lambda = 50$ nm. The assumed value is close to the experimental one determined for bulk Nb (47 nm) [41], but in the layer λ is increased [42]. However, these changes are not significant for layers thicker than 100 nm. The SC strip was placed over the FM layer of thickness $a = 20$ nm and separated from its top surface by the nonmagnetic, nonconducting spacer of thickness $g = 10$ nm; see Fig. 1. The FM layer, made of Ga:YIG, was characterized by the following values of material parameters: saturation magnetization $M_s = 16$ kA/m, exchange stiffness $A_{ex} = 1.37$ pJ/m, and gyromagnetic ratio $\gamma = 179$ GHz/T. The Ga:YIG layer can have a strong PMA [43]. We assumed the realistic value of the uniaxial anisotropy $K_u = 756$ J/m^3, which ensures the out-of-plane orientation of magnetization even in the absence of an external magnetic field. For micromagnetic simulations, we included the magnetization damping constant for Ga:YIG $\alpha = 0.001$. For semianalytical calculations, damping was neglected.

A. Stray field of the superconducting strip

Figures 2(a) and 2(b) present the profiles of the y component [Fig. 2(a)] and x component [Fig. 2(b)] of the stray field $\mathbf{B}_{sc}$ produced by an SC strip of width $w = 400$ nm

for two selected values of the out-of-plane applied field: $B_0 = 30$ mT (black lines) and 90 mT (red lines). The profiles are the x-coordinate dependencies calculated for fixed $y = y_0 = -(t/2 + g + a/2) = -70$ nm, i.e., in the middle of the FM film. The dependencies $B_{sc,y}(x)$, $B_{sc,x}(x)$ are consistent with the expected onionlike shape of the field around the SC strip [see Fig. 1(b)]. The well of $B_{sc,y}(x)$ is a signature of the screening of the external field $\mathbf{B}_0 = B_0\hat{\mathbf{y}}$ by the cost of the increase of the field close to the edges of the strip (vertical dashed lines in Fig. 2). On the other hand, the in-plane component of the stray field $B_{sc,x}$ reflects the deflection of the magnetic field lines bypassing the SC strip. This effect is strongest in the proximity of the strip edges. The stray field was calculated semianalytically using Eqs. (7) [red and black lines in Figs. 2(a) and 2(b)], and the obtained results were successfully cross-checked using FEM calculations [red and black open squares in Figs. 2(a) and 2(b)]. Equations (7) and the plots in Figs. 2(a) and 2(b) show that the stray field scales linearly with the external field B_0. As we increase B_0 from 30 to 90 mT, the magnitudes of the profiles $B_{sc,y}(x)$, $B_{sc,x}(x)$ are increase by a factor of 3 times; see Eqs. (6) and (7).

In the absence of the SC strip, the static magnetization is oriented out of plane due to the PMA in the Ga:YIG layer, but the in-plane component $B_{sc,x}$ tilts the magnetization from the layer's normal; see Fig. 2(c). Surprisingly, the angle between the magnetization and the applied field's direction increases with increasing magnitude of the applied field. However, it is understandable if we keep in mind that the in-plane component of the stray field, which is responsible for the magnetization tilting, increases with the applied field: $B_{sc,x} \propto B_0$; see Fig. 2(b). The angle, at which magnetization is deflected from the out-of-plane direction $\theta_M(x)$ [Fig. 2(c)], can be calculated by finding the minimum of the free energy density (9) for successive positions x. Our calculations have shown that the inhomogeneous exchange interaction caused by noncollinear magnetization texture does not significantly influence the value of the magnetization deviation angle. Therefore, to estimate angle θ_M, we considered the free magnetic energy density of the film in an external magnetic field applied at an angle θ_B, neglecting the exchange interaction:

$$F(\theta) = -BM_s\cos(\theta - \theta_B) + \tfrac{1}{2}\mu_0 M_s\cos^2(\theta) - K_u\cos^2(\theta) \qquad (21)$$

where angle θ is the trial orientation of the magnetization for which we look for a minimum of $F(\theta)$ at every position x independently. The angle $\theta = \theta_M$ corresponding to the minimum $F_{min} = F(\theta_M)$ determines the equilibrium orientation of the magnetization. The first term in Eq. (21) corresponds to the Zeeman interaction with total magnetic field, the second term describes the demagnetizing energy (shape anisotropy), and the third term corresponds to the energy related to the out-of-plane uniaxial anisotropy. It is worth noting that both the magnitude $B(x) = |\mathbf{B}_0 + \mathbf{B}_{sc}(x)|$ and the angle $\theta_B(x) = \arctan\{B_{sc,x}(x)/[B_0 + B_{sc,y}(x)]\}$ of the total static magnetic field are position dependent.

The minimization of Eq. (21) results in an equation for the local magnetization angle $\theta_M(x)$ as a function of the x coordinate. For relatively small values of the angles $\theta - \theta_B$ and θ, the trigonometric functions in Eq. (21) can be expanded in a Taylor series that results in a polynomial equation for θ_M,

$$\frac{1}{\mu_0}B\left[(\theta_M - \theta_B) - \frac{1}{6}(\theta_M - \theta_B)^3\right] + \left(\frac{2K_u}{M_s} - M_s\right)\left[\theta_M - \frac{2}{3}\theta^3\right] = 0, \qquad (22)$$

which is relatively easy to solve. For larger values of the applied field B_0 and related deflection angles, the equilibrium orientation $\theta_M(x)$ must be found numerically. The inset plot of Fig. 2(c) shows the evolution of the maximum angle deviation $\theta_{M,max}$ with the value of the applied magnetic field B_0.

It should be noted that the formation of noncollinear magnetization texture allows SW excitation by an alternating magnetic field applied along the external static field $\mathbf{B}_0$. In this case, the SW modes will only be excited in the regions below the edges of the SC strip, where the static magnetization is tilted. The texture in the FM layer can be modified not only by the strength of the external field B_0, but also by geometrical parameters such as the size and aspect ratio w/t of the SC strip and its separation g from the FM layer.

The London penetration depth λ is a crucial parameter that determines efficiency of the magnetic field screening by the SC material. To understand how λ influences the condition for SW localization, we have calculated the depth of the well $B_{sc,y}(x)$ [see Fig. 2(a)] as a function of λ for the SC strip width $w = 400$ nm and two selected values of the external field: $B_0 = 30$ mT (black lines and open squares) and 90 mT (red line and open squares); see Fig. 3. Semianalytical calculations performed with the help of Eqs. (7) (solid lines) are in perfect agreement with the results of numerical simulations (open squares) for $\lambda > 20$ nm, while for smaller values of λ, semianalytical computations face difficulties. The dependencies $\Delta B_{sc,y}(\lambda)$ are presented in Fig. 3. It is evident that the decrease in $\Delta B_{sc,y}$ with increasing λ is a manifestation of the gradual disappearance of SC properties, which is revealed as a weakening stray field that allows the external field to penetrate deeper into the SC strip. However, this picture becomes more complicated when we consider the more general theory of superconductivity described by the Ginzburg-Landau model that allows phase transitions to mixed and normal phases at the critical fields B_{C1}

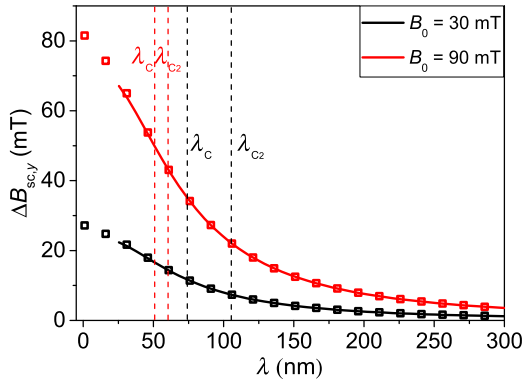

FIG. 3. The depth of the well of the SC field $\Delta B_{sc,y}$ [see Fig. 2(a)] as a function of the London penetration depth λ calculated using Eqs. (7) (solid lines) and numerical simulations (open squares). The black and red lines correspond to two different values of the external field $B_0 = 30$ and 90 mT, respectively. Dashed vertical lines show the critical values of the London penetration depth, λ_C and λ_{C2}, corresponding to the case when the thermodynamic critical field is equal to the external field, $B_C = B_0$, and the transition to the normal state $B_{C2} = B_0$ for $B_0 = 30$ mT (black lines) and 90 mT (red lines), assuming the Ginzburg-Landau parameter $\kappa = 1$.

and B_{C2}, respectively, for type-II superconductors like Nb. Taking into account the dependencies of the critical fields on material parameters (penetration depth λ and correlation length ξ), we should look for the critical values of the material parameters for which the Meissner state or superconductivity is destroyed. To estimate critical values of λ, we have used the general relations between critical fields in a bulk superconductor [44]: $B_{C2} = \Phi_0/(2\pi\xi^2)$ and $B_{C2}/B_C = \kappa\sqrt{2}$, $B_{C1}/B_C < 1$ with Φ_0 the magnetic flux quantum and B_C the thermodynamic critical field. Since giving an approximate analytical formula for B_{C1} is in principle possible for $\kappa \gg 1$ (for Nb, $\kappa = \lambda/\xi \approx 1$ [45]), we can only determine λ_C corresponding to the case $B_C = B_0$, which is an upper estimate for λ_{C1}—i.e., the critical London penetration depth at which $B_{C1} = B_0$. For $B_0 = 30$ mT, $\lambda_{C1} < \lambda_C = 74$ nm and $\lambda_{C2} = 105$ nm (black dashed lines in Fig. 3). This suggests the existence of the Meissner state and the validity of London's theory for $\lambda = \xi = 50$ nm at the field $B_0 = 30$ mT. However, for $B_0 = 90$ mT, we obtain $\lambda_{C1} < \lambda_C = 51$ nm and $\lambda_{C2} = 60$ nm (red dashed lines in Fig. 3), which indicates the possible appearance of a mixed state with vortices. We confirmed this prediction by FEM simulation of the Ginzburg-Landau model (see Appendix D), where we numerically determined $B_{C1} = 53$ mT (32 mT) for the strip of width 400 nm (800 nm) and thickness 100 nm, made of Nb where $\lambda = \xi = 50$ nm. Despite the fact that the system under consideration is in a mixed state for the field $B_0 = 90$ mT, our results will be qualitatively valid for the case of other materials and structures that are able to sustain the Meissner state.

It is also worth noting that the London penetration depth increases with temperature. However, in helium temperatures, this change is less that 3.5% for Nd, where the critical temperature is $T_C = 9.2$ K [45]; see Appendix E for more details.

B. Spin-wave modes confined in the well of the magnetic field induced by a superconducting strip

Figure 4 presents profiles of the SW modes localized in the well of the effective field produced by the SC strip for the external fields $B_0 = 10$ mT [Fig. 4(c)], 30 mT [Figs. 4(a) and 4(d)], and 90 mT [Figs. 4(b) and 4(e)]. The profiles were computed numerically with the help of MUMAX[3] software (red solid lines) and calculated using the semianalytical model (red dashed lines). The blue lines show the FMR frequency of the homogeneous film at certain B_0 fields in the absence of the SC strip. The left and right columns of Fig. 4 correspond to SC strip widths of $w = 400$ nm [Figs. 4(a) and 4(b)] and 800 nm [Figs. 4(c), 4(d), and 4(e)], respectively. For larger values of the external field B_0, the well $B_{sc,y}(x)$ is deeper [see Fig. 2(a)] and can accommodate more SW modes. However, there is an upper limit for B_0 caused by the phase transition at B_{C1}. Our model, based on London's theory, does not include the existence of a mixed state, which can appear in the considered range of the external field B_0. The presence of vortices will modify the stray field produced by the SC strip that will be important in the experimental implementation of the investigated system. However, the ultimate limit is given by B_{C2} [46]. On the other hand, the field $B_0 = 10$ mT is too small for the strip of width 400 nm to create a well that is deep enough to confine SW modes. For the external field $B_0 = 30$ mT [Fig. 4(a)] or 90 mT [Fig. 4(b)], the well is sufficiently deep to bind one or two SW modes (solid and dashed lines) of the frequencies lower than the FMR frequency of the homogeneous film (horizontal blue line). Another strategy for SW binding is to widen the SC strip and thus widen the related well of the stray field.

In Figs. 4(c)–4(e), for $w = 800$ nm, we observe a larger number of localized SW modes, which is the result of two factors: (i) the frequency difference between SW-mode energy levels becomes smaller due to the widening of the well (the main factor) and (ii) the depth of the well is slightly increased with the widening of the SC strip (e.g., for $w = 800$ nm, $\Delta B_{sc,y}$ is about 1.4 times larger than for $w = 400$ nm). Thus, for $w = 800$ nm, there are one, two, and four localized modes for $B_0 = 10$ mT [Fig. 4(c)], 30 mT [Fig. 4(d)], and 90 mT [Fig. 4(e)], respectively. It should be noted that the approximation of the well $B_{sc,y}(x)$ by a parabolic well (13) is valid in the considered system only for a finite range of widths w (around 350 nm), while for much smaller or larger widths, the terms higher than quadratic must be included in expansion (13). For example, for $w = 400$ nm and 800 nm, the approximation of

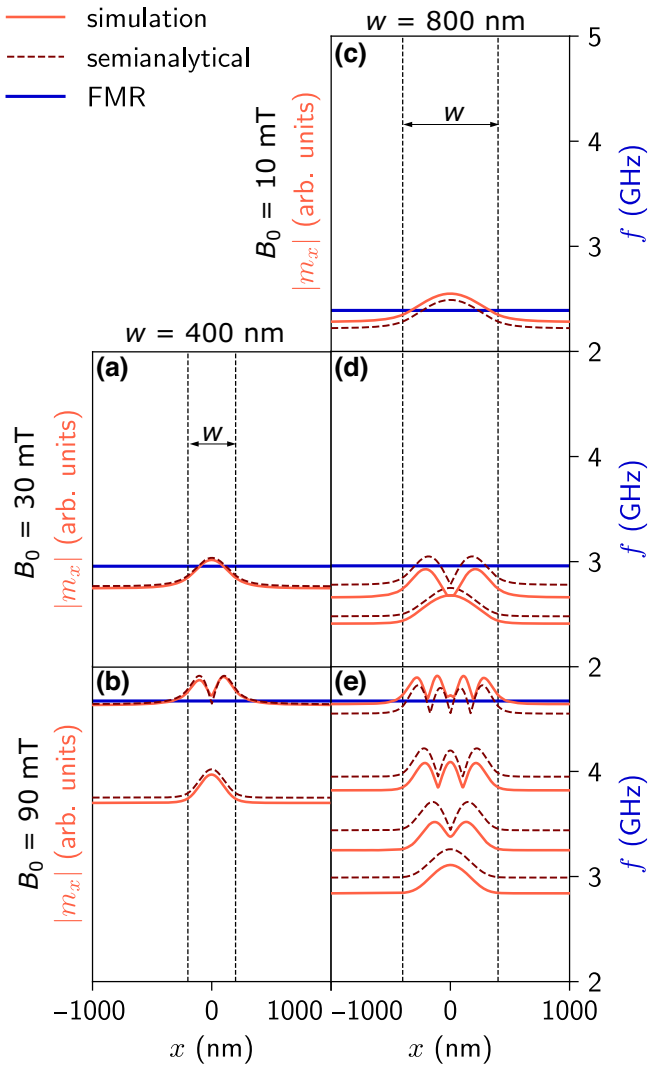

FIG. 4. The profiles of the SW modes localized in the effective field well produced by the SC strip for external field values $B_0 = 10$ mT (c), 30 mT (a),(d), and 90 mT (b),(e) obtained from micromagnetic simulations using the MUMAX^3 environment (red solid lines) and the results of the semianalytical model (red dashed lines). The blue lines show the FMR frequency of a homogeneous film for a given external magnetic field B_0 value in the absence of the SC strip. The left and right columns correspond to SC widths $w = 400$ nm and 800 nm, respectively. Vertical black dashed lines indicate the position of the SC strip edges. All plots share the same frequency and space scales and the amplitude of the modes is normalized to enhance readability of the plot (the difference between the results obtained by the semianalytical approach and micromagnetic simulations is shown by the offset in the plot).

$B_{sc,y}$ requires including up to fourth- and sixth-order terms, respectively. The semianalytical results (dashed lines) are in relatively good agreement with the numerical solution of the LL equation obtained using the MUMAX^3 environment (solid lines). Because of the presence of higher-order terms in $B_{sc,y}$, the SW modes are not equidistant, in contrast to the eigenfunctions of the quantum harmonic oscillator, i.e., Hermitian functions. However, our mode profiles can be approximated by Hermitian functions with fitting parameter β_2 in Eq. (15). This trick allowed us to simplify the averaged demagnetizing field to a compact form (18) (see Appendix C) and easily find the eigenfrequencies (17).

The dependence of the frequencies of the localized SW modes on the external magnetic field is presented in Fig. 5 for SC strip widths $w = 400$ nm [Fig. 5(a)] and 800 nm [Fig. 5(b)]. The results of the semianalytical calculations and micromagnetic simulations are marked by solid lines and open symbols, respectively. As mentioned in the previous paragraph, the number of localized modes increases with increasing external field value and the width of the SC strip. In general, the results of the theoretical calculations and micromagnetic simulations are in good agreement. The discrepancies are larger for the strip width $w = 800$ nm than for 400 nm and they increase with increasing external

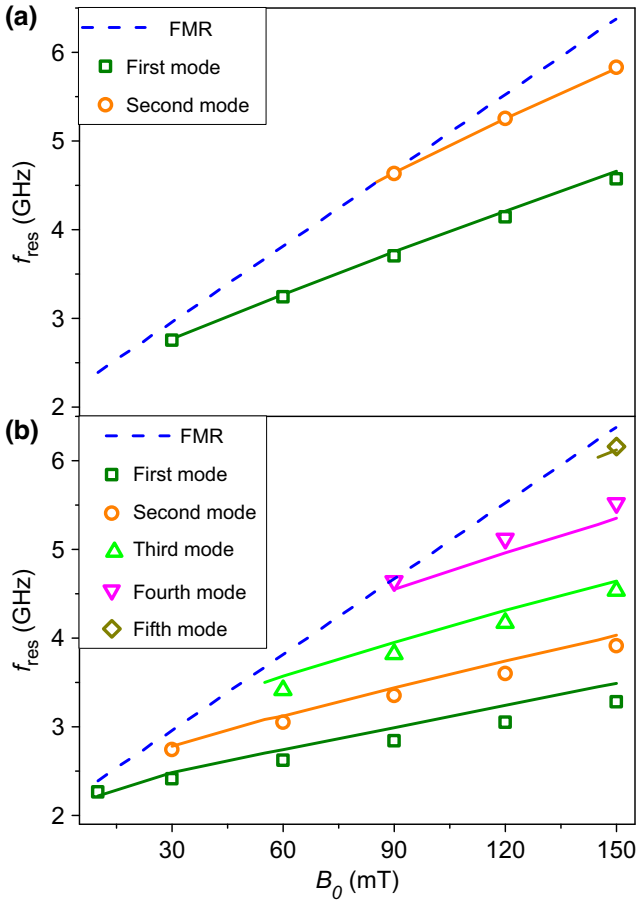

FIG. 5. The dependence of the localized SW modes on the external magnetic field B_0 for systems with SC strip widths $w = 400$ nm (a) and $w = 800$ nm (b). The solid lines and open symbols correspond to the semianalytical calculations and micromagnetic simulations, respectively. Dashed lines show the FMR frequency of the uniformly magnetized film.

magnetic field. This can be related to the simplifications underlying our theoretical model, according to which we have neglected the tangential component of the field produced by the SC strip $B_{sc,x}$, which slightly deflects the static magnetization from the normal to the FM layer and forms a noncollinear magnetization structure in the vicinity of the SC-strip edges [see Fig. 2(c)]. In our model, we have considered the uniform magnetization ground state where the FM layer is magnetized out of plane. This assumption is reasonable because the magnetization deviation angle θ_M is relatively small for a narrow strip, while for a wider strip, the deviation angle is larger and increases significantly for large external field values. To prove that this is the main reason for the discrepancies between the micromagnetic simulations and the semianalytical model, we have performed micromagnetic simulations with $B_{sc,x} = 0$, which showed results much closer to the theoretical calculations. Small differences can also be caused by the use of the diagonal approximation in our theory. However, the diagonal elements of the dynamical demagnetization field are quite small, which means that nondiagonal elements can be really neglected because they are usually smaller than diagonal elements.

IV. CONCLUSIONS

We examined a superconductor-ferrimagnet hybrid planar nanostructure wherein a flat SC strip is situated above a uniform FM layer, while the external field is applied out of plane. In this configuration, the flat SC strip, being in a Meissner state, produces a stray field that reduces the static effective field inside the thin FM layer placed below. When the FM layer is made of soft magnetic material with PMA, the SW modes can be confined within the region of lowered field (i.e., in the well of the internal field). These modes have frequencies lower than the FMR frequency of the FM layer, which explains their exponential decay outside the region of the well. By adjusting the value of the uniform external field, we can control the depth of the well and modify the number and frequencies of the confined SW modes. This outcome is difficult to achieve in the conventional magnonic nanostructures where the stray field, as a result of demagnetization, depends on the geometry and magnetic configuration. The first is determined at the fabrication stage and the latter can be modified by an external field, but its full control requires strong fields due to large demagnetization effects in planar structures.

Our work integrates the numerical and semianalytical studies. The analytical approach is computationally undemanding and provides deep insight into the magnetization dynamics and the mechanism of SW localization in dipolarly coupled superconductor-ferrimagnet systems. The presented ideas can be used to design superconductor-ferrimagnet hybrid devices for on-demand control of SW localization and propagation.

Data supporting this study are openly available from Zenodo [47].

ACKNOWLEDGMENTS

The authors would like to thank M. Silaev, O. Dobrovolskiy, O. Tartakivska, and M. Zelent for fruitful discussions. The work was supported by the National Science Center, Poland under Grants No. UMO-2019/35/D/ST3/03729, No. UMO-2021/43/I/ST3/00550, and No. UMO-2021/41/N/ST3/04478. The numerical simulations were performed at Poznań Supercomputing and Networking Center (Grant No. pl0095-01). K. Sobucki is a scholarship recipient of the Adam Mickiewicz University Foundation for the academic year 2023/2024.

APPENDIX A: STRAY FIELD GENERATED BY MAGNETIZATION TEXTURE IN THE FM LAYER—MICROMAGNETIC STUDIES

The stray field generated by SC eddy currents influences the FM layer, which is also manifested by the formation of a weak magnetization texture. We calculated the stray field produced by this texture to assess its impact on the SC strip. The calculations were done using micromagnetic simulations in the MUMAX^3 environment, with the external field $B_0 = 90$ mT applied along the y axis. The stray field distributions are presented in Fig. 6 for strips of widths (a) 400 nm and (b) 800 nm. In both cases, the magnitude of the stray field is smaller than 1% of the external field value; thus, its influence on the SC system can be neglected and, therefore, the complicated self-consistent problem can be reduced to necessity to take into account only the impact of the SC strip on the FM layer.

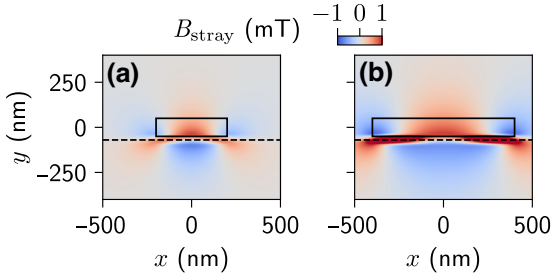

FIG. 6. The micromagnetic simulations of the stray field generated by the magnetization texture in the FM layer of thickness 20 nm. The texture is induced by infinitely long SC strips of thickness 100 nm and widths (a) 400 nm and (b) 800 nm (separated from the FM film by the 10-nm air gap), placed in the external field $B_0 = 90$ mT applied in the y direction. The black rectangle indicates the position of the SC strip and the dashed black line marks the center of the FM film. In both (a) and (b) the magnitude of the stray field is less than 1% of the external field value, so its influence on the system can be neglected. The material parameters for the FM film are the same as in the main text. The London penetration depth for the SC strip is $\lambda = 50$ nm.

APPENDIX B: DISPERSION RELATION—DERIVATION

The dispersion relation can be derived from Eqs. (12) after introducing the average of the dipolar field (dipolar operator) in a way similar to the approach known in quantum mechanics. Let us express each SW mode by a function from the orthonormal base, $m_{p,n}(x) \approx C_p M_s \psi_n(Kx)$, as in Eq. (15). When we introduce the norm $\langle \psi_n^2 \rangle := \int_V dv |\psi_n(Kx)|^2 = ab/K$, and then multiply both Eqs. (12) by $\psi_n^*(Kx)$ and integrate them over the whole volume of the magnetic system, we obtain

$$i\omega\, C_x \langle \psi_n^2 \rangle = C_z \langle \psi_n | \Xi(x) | \psi_n \rangle - |\gamma| \mu_0 \langle h_{d,z} \rangle_n, \quad \text{(B1a)}$$

$$-i\omega\, C_z \langle \psi_n^2 \rangle = C_x \langle \psi_n | \Xi(x) | \psi_n \rangle - |\gamma| \mu_0 \langle h_{d,x} \rangle_n, \quad \text{(B1b)}$$

where $\langle h_{d,p} \rangle_n := \int_V dv \psi_n^*(Kx) h_{d,p}(x)$ for $p = \{x, y\}$ can be considered as an averaged component of the dynamic demagnetizing field. This definition is clear when we note that the field $h_{d,p,n}$ is the result of an action of the integral operator on $\psi_n(Kx)$ [strictly related to the magnetization $m_{p,n}(x)$]; see Eq. (16). Taking into account the fact that the $\psi_n(Kx)$ are eigenfunctions of the operator $\Xi(x)$ with eigenvalues $\omega_{0,n}$, but not of the dynamical demagnetizing field operator, Eqs. (B1) can be rewritten as

$$i\omega\, C_x = C_z(\omega_{0,n} - |\gamma| \mu_0 M_s \langle \tilde{h}_{d,z} \rangle_n), \quad \text{(B2a)}$$

$$-i\omega\, C_z = C_x(\omega_{0,n} - |\gamma| \mu_0 M_s \langle \tilde{h}_{d,x} \rangle_n), \quad \text{(B2b)}$$

where $\langle \tilde{h}_{d,p} \rangle_n = 1/(C_p M_s) \langle h_{d,p} \rangle$ is a dimensionless averaged field (see Appendix C). The homogeneous set of equations (B2) gives nontrivial solution for the resonance frequency ω_n when

$$\begin{vmatrix} i\omega & \omega_{0,n} - |\gamma| \mu_0 M_s \langle \tilde{h}_{d,z} \rangle_n \\ \omega_{0,n} - |\gamma| \mu_0 M_s \langle \tilde{h}_{d,x} \rangle_n & -i\omega \end{vmatrix} = 0, \quad \text{(B3)}$$

which leads to the dispersion relation shown in Eq. (17).

APPENDIX C: AVERAGED DIPOLAR FIELD—DERIVATION

For every nth SW mode $\mathbf{m}_n(x)$ (confined in the well of the stray field), the dynamical demagnetizing field $\mathbf{h}_{d,n}(x)$ [related to own dynamics of $\mathbf{m}_n(x)$] is given by Eq. (16). The field $\mathbf{h}_{d,n}(x)$ can be considered as a result of the action of the integral operator on magnetization $\mathbf{m}_n$. When we approximate $\mathbf{m}_n$ by function $\psi_n(Kx)$ from the orthonormal set, $m_{p,n}(x) \approx C_p M_s \psi_n(Kx)$ [see Eq. (15)], and integrate $\mathbf{h}_{d,n(x)}$ over the whole volume with $\psi_n(Kx)$, we obtain the average value of the dipolar field operator:

$$\langle h_{d,p} \rangle_n = -M_s \sum_q C_q \int_V \int_{V'} dv\, dv' \psi_n(Kx) \psi_n(Kx') \times \frac{d^2}{dp\, dq'} \frac{1}{4\pi |\mathbf{r} - \mathbf{r}'|}. \quad \text{(C1)}$$

Here the indices p and q run over the coordinates x and z, and the derivative d/dq' means d/dx' (or d/dz') for $q = x$ (or $q = z$). Each of the integrals in (C1) is actually a threefold integral: $\int_{-\infty}^{\infty} dx \int_{y_0 - a/2}^{y_0 + a/2} dy \int_{-b/2}^{b/2} dz$ with $y_0 = -(t/2 + g + a/2)$. This problem can be simplified when we express the function $1/4\pi|\mathbf{r} - \mathbf{r}'|$ in Fourier space for the wave vector $\mathbf{k} = k_x \hat{\mathbf{x}} + k_z \hat{\mathbf{z}}$ [48], i.e.,

$$\frac{1}{4\pi |\mathbf{r} - \mathbf{r}'|} = \frac{1}{2\pi} \int_{-\infty}^{\infty} \int_{-\infty}^{\infty} dk_x\, dk_z \frac{1}{k} e^{-k|y - y'|} \times e^{ik_x(x - x')} e^{ik_z(z - z')}, \quad \text{(C2)}$$

where $k = \sqrt{k_x^2 + k_y^2}$, and then use the identities

$$\int_{y_0 - a/2}^{y_0 + a/2} \int_{y_0 - a/2}^{y_0 + a/2} dy\, dy' \frac{1}{k} e^{-k|y - y'|} = \frac{2a}{k} \left(1 - \frac{1 - e^{-ka}}{ka}\right),$$

$$\int_{-b/2}^{b/2} \int_{-b/2}^{b/2} dz\, dz' e^{ik_z(z - z')} = 2\pi b \delta(k_z) \quad \text{for } b \to \infty.$$

This allows us to express Eq. (C1) in the form

$$\langle h_{d,p} \rangle_n = -M_s \frac{ab}{K^2} \sum_q C_q \int dk_x \left[\int dk_z \frac{k_p k_q}{k^2} \times \left(1 - \frac{1 - e^{ka}}{ka}\right) \delta(k_z)\, \tilde{\psi}_n^2 \left(\frac{k_x}{K}\right) \right]. \quad \text{(C3)}$$

One can note that $\langle h_{d,z} \rangle_n = 0$ and $\langle h_{d,x} \rangle_n$ contains only the term for $p = x$. In the linear regime, the dynamic demagnetizing field scales linearly with the SW amplitude; therefore, it is useful to introduce the normalized dimensionless average field

$$\langle \tilde{h}_{d,x} \rangle_n = \frac{1}{C_x M_s} \langle h_{d,x} \rangle_n, \quad \text{(C4)}$$

where $C_x M_s$ is an SW amplitude in A/m. Finally, Eqs. (C3) and (C4) lead to Eq. (18).

APPENDIX D: STRAY FIELD GENERATED BY THE SC STRIP: THE LONDON VERSUS GINZBURG-LANDAU THEORY—FEM STUDIES

The Ginzburg-Landau (GL) theory is a generalization of the London theory of superconductivity. The use of

the London theory in this paper is justified by its relative simplicity, which allows semianalytical calculations. However, the London theory does not predict the existence of the critical fields B_{C1} and B_{C2}, which are associated with the emergence of a mixed state (with magnetic vortices) and the complete disappearance of superconductivity, respectively. Therefore, we should investigate whether it is rational to consider the Meissner state in our system for the assumed value of the London penetration depth $\lambda = 50$ nm.

We used COMSOL Multiphysics® solve dimensionless time-dependent GL equations in the SC domain [49–51]:

$$\eta \frac{\partial \Psi}{\partial t} = -\left(\frac{i}{\kappa}\nabla + \mathbf{A}\right)^2 \Psi + (1-|\Psi|^2)\Psi, \tag{D1a}$$

$$\sigma \frac{\partial \mathbf{A}}{\partial t} = \frac{1}{2i\kappa}(\Psi^* \nabla \Psi - \Psi \nabla \Psi^*) - |\Psi|^2 \mathbf{A} - \nabla \times \nabla \times \mathbf{A}. \tag{D1b}$$

Here $\Psi = \Psi(\mathbf{r}, t)$ is the order parameter, σ represents the electric conductivity of the normal (non-SC) state, while η denotes the normalized friction coefficient. Since we have focused on the steady state of the system ($t \to \infty$) rather than its dynamics, the choice of specific values of σ and η for the dimensionless GL equation is not relevant once we are able to reach the same steady state. Outside the SC strip (in the vacuum) $\Psi = 0$, $\sigma = 0$, and the vector potential was determined from the equation

$$\nabla \times \nabla \times \mathbf{A} = 0. \tag{D2}$$

To ensure that the GL equations are well defined, the gauge must be fixed. We have chosen the gauge with zero electric potential, which turns out to be the most convenient choice for Eqs. (D1).

We set the boundary conditions at the interface between the SC and vacuum as $\nabla\Psi \cdot \mathbf{n} = 0$ and $\mathbf{A} \cdot \mathbf{n} = 0$ [49]. The vacuum domain is large in size but finite. We assumed that the SC stray field on its boundaries equals zero and that the total field $\mathbf{B} = B_0\hat{\mathbf{y}}$, which leads to the boundary condition $\nabla \times \mathbf{A} = B_0\hat{\mathbf{y}}$ [49]. We solved Eqs. (D1) and (D2) using a 2D model, i.e., assuming that $\mathbf{A}(x, y)$ and $\Psi(x, y)$ are

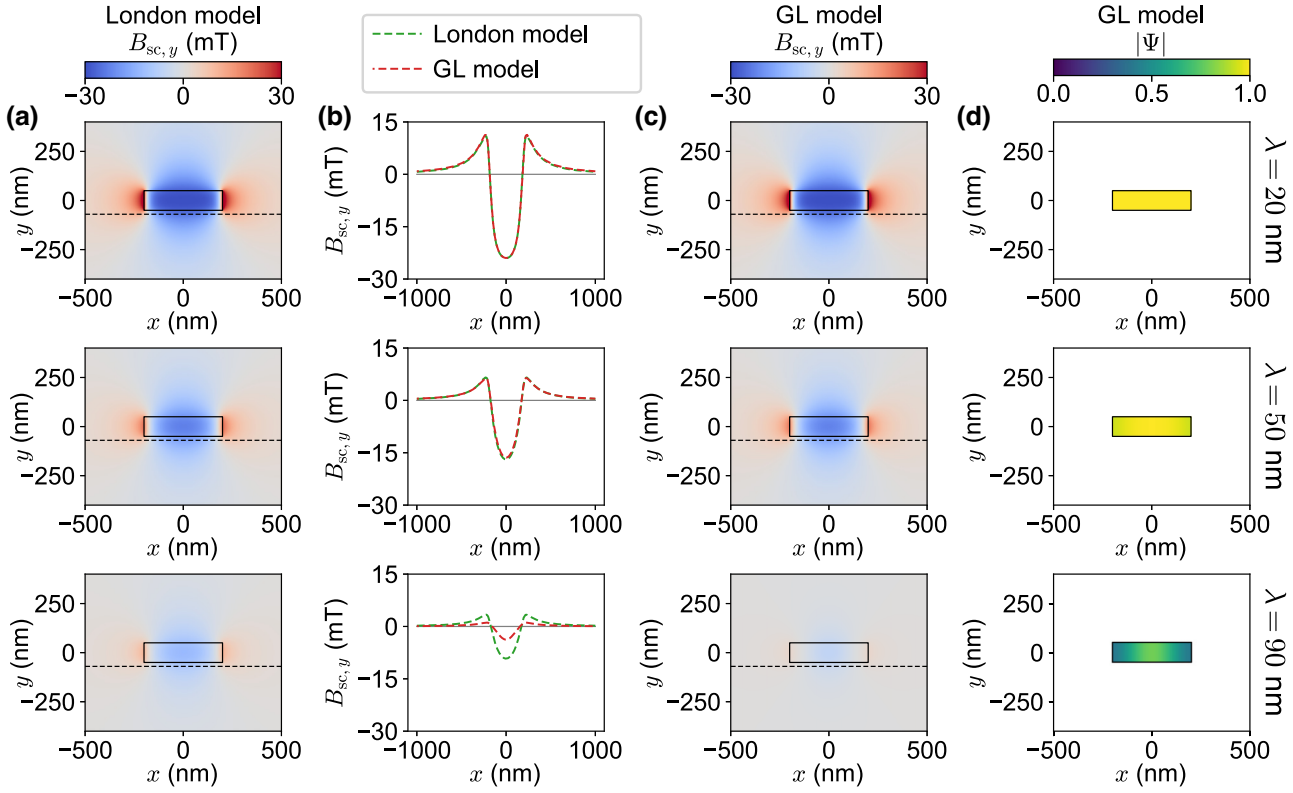

FIG. 7. The FEM solutions of the GL and London equations for an infinitely long SC strip of thickness 100 nm and width 400 nm. The calculations were performed for different penetration depths $\lambda = 20, 50$, and 90 nm. For simplicity, we assumed a correlation length of $\xi = \lambda$, which leads to $\kappa = 1$. The value of the external field $\mathbf{B}_0 = B_0\hat{\mathbf{y}}$ has been set to 30 mT. (a) The London model: the y component of the stray field $B_{sc,y}$ on the x-y plane inside the SC strip and in the surrounding nonmagnetic and nonconducting domain. The dashed black line indicates the center of the FM layer. (b) The y component of the stray field $B_{sc,y}(x)$ obtained from the London and GL models in the center of the FM layer ($y = -70$ nm). (c) The GL model: $B_{sc,y}$ on the x-y plane inside the SC strip and in the surrounding nonmagnetic and nonconducting domain. The dashed black line indicates the center of the FM layer. (d) The GL model: the modulus of the order parameter $|\Psi|$ in the SC domain.

homogeneous along the strip. The transitions from dimensionless to realistic quantities are described by the transformations $(x, y, z) \to (x/\lambda, y/\lambda, z/\lambda)$, $t \to t/(\mu_0 \lambda \sigma)$, and $\mathbf{A} \to 2e\xi\mathbf{A}/\hbar$.

In this paper, we consider a 2D system and assume its homogeneity in the z direction. This assumption is not valid in the mixed state with the field applied in the y direction, where the induced vortices disturb the mentioned homogeneity. For this reason, the first critical field must be estimated numerically using a 3D model. This gives us the range of the applied field in which we are still in the Meissner state for a given value of λ (assuming that we are working with a $\kappa \approx 1$ superconductor), and we can investigate the system using London's model.

1. Two-dimensional simulations

We start with 2D simulations based on the GL model, which should give an insight into the reduction of the stray field associated with the change in the density of the Cooper pairs, which is not included in the London model.

Figure 7 shows the difference between the 2D GL and London models for fixed external field $B_0 = 30$ mT and three selected penetration depths, $\lambda = 20$, 50, 90 nm. In our studies, we fixed the GL parameter $\kappa = \lambda/\xi = 1$, which is equivalent to $\xi = \lambda$ (this choice is in the range of κ for bulk Nb). For small values of λ (and ξ), both models give consistent results. For $\lambda = 20$ nm, the difference between the models is negligible. For $\lambda = 50$ nm, used in the manuscript for the studies of confined SW modes, the differences in the stray field (calculated from the GL and London models) are still barely distinguishable; see the middle plot of Fig. 7(b). For $\lambda = 50$ nm, $|\Psi| \approx 1$ in the whole volume of the SC strip except for a small reduction near its lateral edges [see the middle plot of Fig. 7(c)], which means that we are still in the Meissner state, i.e., the external field is still below the first critical field: $B_0 < B_{C1}$. For $\lambda = 90$ nm, the discrepancy between the London and GL models becomes significant. The stray field produced by the SC is about 2 times smaller in the GL model, see the bottom plot of Fig. 7(b). At the same time, $|\Psi|$ is strongly reduced; see the bottom plot of Fig. 7(d).

Figure 8 is analogical to Fig. 3 in the main part of the manuscript. It shows the depth of the well of the SC field for the London and GL models at 30 mT. For comparison, we used two values of κ: 1 and 10. Up to $\lambda \approx 50$ nm, the well depth for all systems is almost the same. For $\lambda > 50$ nm, it starts to decrease much stronger for the GL model with $\kappa = 1$, reaching zero at the critical value of $\lambda = \xi = 115$ nm. Such an effect is understandable if we note that, as the second critical magnetic field $B_{C2} \propto 1/\xi^2$, the increase in λ (for constant κ) leads to a reduction in B_{C2}. At $B = B_{C2}$, the order parameter goes to zero, leading to the disappearance of superconductivity. Such a phase transition is not observed in the London model, which lacks any kind of critical field. Interestingly, if we increase κ to 10, the results are in agreement with the London model, showing that, for large values of κ, it gives reliable results for a wide range of λ.

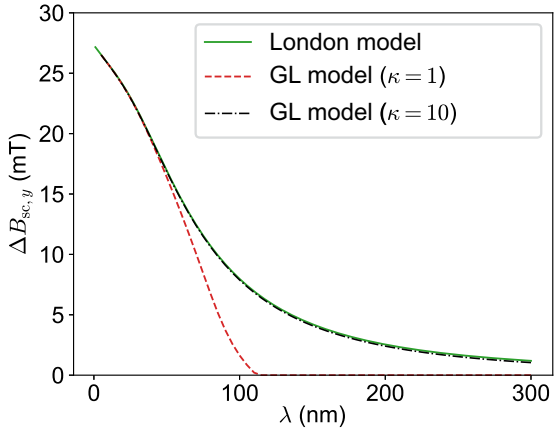

FIG. 8. The depth of the well of the SC field $\Delta B_{sc,y}$ (at the external field $B_0 = 30$ mT) as a function of the penetration length λ calculated using the London model (solid green line) and GL model for $\kappa = 1$ (dashed red line) and $\kappa = 10$ (dash-dot black line).

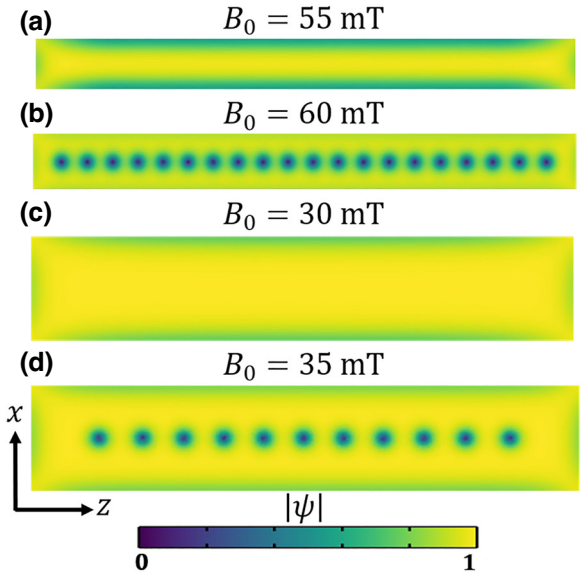

FIG. 9. FEM simulations of the GL model of the nucleation of magnetic vortices in the finite SC strip with length 4000 nm and thickness 100 nm. We investigated strips of two different widths: (a),(b) 400 nm and (c),(d) 800 nm. For the narrower (wider) strip, the transition to a mixed state is observed at $B_{C1} \approx 53$ mT ($B_{C1} \approx 32$ mT). The modulus of the order parameter $|\Psi|$ is plotted in the x-z plane in the centers of the strips ($y = 0$) for the external field value slightly below (a),(c) and slightly above (b),(d) B_{C1}. We assume that $\lambda = \xi = 50$ nm.

2. Three-dimensional simulations

To observe the nucleation of vortices, we solved the GL equations using FEM simulations for the SC strips of finite length (4000 nm), which differ in width (400 and 800 nm) and have the same thickness (100 nm). Figure 9 presents the distribution of the modulus of the order parameter $|\Psi|$ along the strips and across their widths (i.e., in the x-z plane). We can see the transition from the Meissner state [Figs. 9(a) and 9(c)] to the mixed state [Figs. 9(b) and 9(d)], where a single row of Abrikosov vortices appears in the center of the nanowire at higher fields. The numerically estimated value of the first critical field B_{C1} is larger for the narrower strip (53 mT) than for the wider one (32 mT).

The appearance of vortices allows the external field to penetrate into the superconductor, which significantly reduces the stray field produced by the SC strip. It makes the SW binding much more difficult. Since vortices generate inhomogeneity along the strip axis, the problem cannot be treated as quasi-one-dimensional for SWs, which may be the subject of a new study.

APPENDIX E: TEMPERATURE AND FIELD DEPENDENCE OF THE LONDON PENETRATION DEPTH

For practical reasons, it is also worth studying how the London penetration depth changes with temperature T and external field B_0. For a rough estimation of the $\lambda(T)$ dependence, the general formula based on a two-fluid model [44,52] can be used:

$$\lambda(T) = \lambda(0)\frac{1}{1-(T/T_C)^4}. \tag{E1}$$

In the wide range of temperatures $0 < T < T_C/2$, the relative change $[\lambda(T) - \lambda(0)]/\lambda(0)$ is about 3.3%; see Fig. 10. It is worth noting that, for Nb ($T_C = 9.2$ K), $T_C/2$ is close to the helium boiling temperature.

The London penetration depth depends weakly on the applied field B_0 for low temperature $T < T_C/2$. For most of the superconductors [53,54], the dependence $\lambda(B_0)$ exhibits an slight increase, quadratic in B_0, which can be ignored in our study.

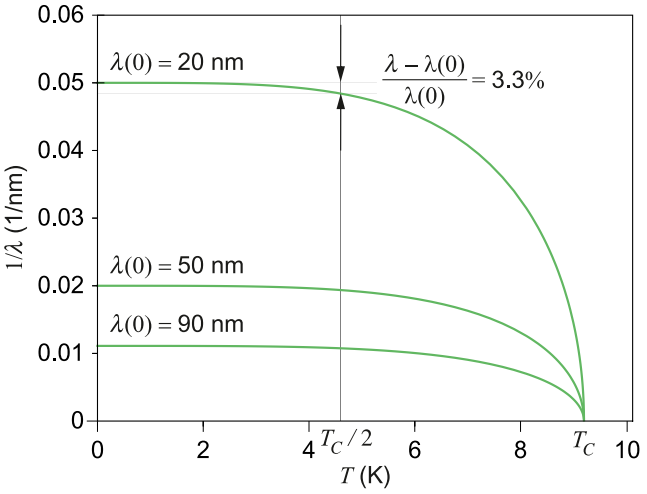

FIG. 10. The temperature dependence of the inverse of the London penetration depth $1/\lambda(T)$. We used Eq. (E1) for three (considered in Fig. 7) values of London penetration depths at $T = 0$, $\lambda(0) = 20, 50, 90$ nm, and for a fixed critical temperature $T_C = 9.2$ K, characteristic for Nb. In the wide temperature range $T < T_C/2$, $\lambda(T)$ changes less than 3.3%.

[1] S. Ran, C. Eckberg, Q.-P. Ding, Y. Furukawa, T. Metz, S. R. Saha, I.-L. Liu, M. Zic, H. Kim, J. Paglione, and N. P. Butch, Nearly ferromagnetic spin-triplet superconductivity, Science **365**, 684 (2019).

[2] S. S. Saxena, P. Agarwal, K. Ahilan, F. M. Grosche, R. K. W. Haselwimmer, M. J. Steiner, E. Pugh, I. R. Walker, S. R. Julian, P. Monthoux, G. G. Lonzarich, A. Huxley, I. Sheikin, D. Braithwaite, and J. Flouquet, Superconductivity on the border of itinerant-electron ferromagnetism in UGe_2, Nature **406**, 587 (2000).

[3] S. Sinha, G. Crabtree, D. Hinks, and H. Mook, Study of coexistence of ferromagnetism and superconductivity in single crystal $ErRh_4B_4$, Physica B+C **109-110**, 1693 (1982), 16th International Conference on Low Temperature Physics, Part 3.

[4] C. Bernhard, J. L. Tallon, C. Niedermayer, T. Blasius, A. Golnik, E. Brücher, R. K. Kremer, D. R. Noakes, C. E. Stronach, and E. J. Ansaldo, Coexistence of ferromagnetism and superconductivity in the hybrid ruthenate-cuprate compound $RuSr_2GdCu_2O_8$ studied by muon spin rotation and dc magnetization, Phys. Rev. B **59**, 14099 (1999).

[5] I. F. Lyuksyutov and V. L. Pokrovsky, Ferromagnet–superconductor hybrids, Adv. Phys. **54**, 67 (2005).

[6] J. Linder and J. W. A. Robinson, Superconducting spintronics, Nat. Phys. **11**, 307 (2015).

[7] A. Bespalov, Electromagnetic proximity effect in superconductor/ferromagnet bilayers with in-plane magnetic texture, Phys. C: Supercond. **595**, 1354032 (2022).

[8] R. Cai, I. Žutić, and W. Han, Superconductor/ferromagnet heterostructures: A platform for superconducting spintronics and quantum computation, Adv. Quantum Technol. **6**, 2200080 (2023).

[9] F. S. Bergeret, A. F. Volkov, and K. B. Efetov, Long-range proximity effects in superconductor-ferromagnet structures, Phys. Rev. Lett. **86**, 4096 (2001).

[10] Y. A. Genenko, A. Usoskin, and H. C. Freyhardt, Large predicted self-field critical current enhancements in superconducting strips using magnetic screens, Phys. Rev. Lett. **83**, 3045 (1999).

[11] M. V. Milošević, G. R. Berdiyorov, and F. M. Peeters, Mesoscopic field and current compensator based on a

hybrid superconductor-ferromagnet structure, Phys. Rev. Lett. **95**, 147004 (2005).

[12] V. K. Vlasko-Vlasov, F. Colauto, A. I. Buzdin, D. Rosenmann, T. Benseman, and W.-K. Kwok, Magnetic gates and guides for superconducting vortices, Phys. Rev. B **95**, 144504 (2017).

[13] I. A. Golovchanskiy, N. N. Abramov, V. S. Stolyarov, V. V. Bolginov, V. V. Ryazanov, A. A. Golubov, and A. V. Ustinov, Ferromagnet/superconductor hybridization for magnonic applications, Adv. Funct. Mater. **28**, 1802375 (2018).

[14] M. Borst, P. H. Vree, A. Lowther, A. Teepe, S. Kurdi, I. Bertelli, B. G. Simon, Y. M. Blanter, and T. van der Sar, Observation and control of hybrid spin-wave–Meissner-current transport modes, Science **382**, 430 (2023).

[15] I. A. Golovchanskiy, N. N. Abramov, V. S. Stolyarov, P. S. Dzhumaev, O. V. Emelyanova, A. A. Golubov, V. V. Ryazanov, and A. V. Ustinov, Ferromagnet/superconductor hybrid magnonic metamaterials, Adv. Sci. **6**, 1900435 (2019).

[16] M. A. Kuznetsov and A. A. Fraerman, Temperature-sensitive spin-wave nonreciprocity induced by interlayer dipolar coupling in ferromagnet/paramagnet and ferromagnet/superconductor hybrid systems, Phys. Rev. B **105**, 214401 (2022).

[17] A. Ghirri, C. Bonizzoni, M. Maksutoglu, A. Mercurio, O. Di Stefano, S. Savasta, and M. Affronte, Ultrastrong magnon-photon coupling achieved by magnetic films in contact with superconducting resonators, Phys. Rev. Appl. **20**, 024039 (2023).

[18] A. Ghirri, C. Bonizzoni, M. Maksutoglu, and M. Affronte, Interplay between magnetism and superconductivity in a hybrid magnon-photon bilayer system, arXiv:.2312.02785 [cond-mat.supr-con].

[19] T. Yu and G. E. W. Bauer, Efficient gating of magnons by proximity superconductors, Phys. Rev. Lett. **129**, 117201 (2022).

[20] X.-H. Zhou and T. Yu, Gating ferromagnetic resonance of magnetic insulators by superconductors via modulating electric field radiation, Phys. Rev. B **108**, 144405 (2023).

[21] I. A. Golovchanskiy, N. N. Abramov, V. S. Stolyarov, A. A. Golubov, V. V. Ryazanov, and A. V. Ustinov, Nonlinear spin waves in ferromagnetic/superconductor hybrids, J. Appl. Phys. **127**, 093903 (2020).

[22] O. V. Dobrovolskiy, R. Sachser, T. Brächer, T. Böttcher, V. V. Kruglyak, R. V. Vovk, V. A. Shklovskij, M. Huth, B. Hillebrands, and A. V. Chumak, Magnon–fluxon interaction in a ferromagnet/superconductor heterostructure, Nat. Phys. **15**, 477 (2019).

[23] B. Niedzielski, C. Jia, and J. Berakdar, Magnon-fluxon interaction in coupled superconductor/ferromagnet hybrid periodic structures, Phys. Rev. Appl. **19**, 024073 (2023).

[24] A. Shekhter, L. N. Bulaevskii, and C. D. Batista, Vortex viscosity in magnetic superconductors due to radiation of spin waves, Phys. Rev. Lett. **106**, 037001 (2011).

[25] O. V. Dobrovolskiy and A. V. Chumak, Nonreciprocal magnon fluxonics upon ferromagnet/superconductor hybrids, J. Magn. Magn. Mater. **543**, 168633 (2022).

[26] O. V. Dobrovolskiy, Q. Wang, D. Y. Vodolazov, B. Budinska, S. Knauer, R. Sachser, M. Huth, and A. I. Buzdin, Cherenkov radiation of spin waves by ultra-fast moving magnetic flux quanta, arXiv:2103.10156 [cond-mat.other].

[27] V. V. Schmidt, *The Physics of Superconductors: Introduction to Fundamentals and Applications* (Springer Verlag, Berlin-Heidelberg-New York, 1997).

[28] M. C. Fiolhais and H. Essén, Magnetic field expulsion from an infinite cylindrical superconductor, Phys. C: Supercond. **497**, 54 (2014).

[29] A. Badía and H. C. Freyhardt, Meissner state properties of a superconducting disk in a non-uniform magnetic field, J. Appl. Phys. **83**, 2681 (1998).

[30] E. H. Brandt, Thin superconductors in a perpendicular magnetic ac field: General formulation and strip geometry, Phys. Rev. B **49**, 9024 (1994).

[31] E. H. Brandt, Thin superconductors in a perpendicular magnetic ac field. II. Circular disk, Phys. Rev. B **50**, 4034 (1994).

[32] A. Gurevich and G. Melkov, *Magnetization Oscillations and Waves* (CRC Press, London, 1996).

[33] G. N. Kakazei, P. E. Wigen, K. Y. Guslienko, V. Novosad, A. N. Slavin, V. O. Golub, N. A. Lesnik, and Y. Otani, Spin-wave spectra of perpendicularly magnetized circular submicron dot arrays, Appl. Phys. Lett. **85**, 443 (2004).

[34] G. N. Kakazei, G. R. Aranda, S. A. Bunyaev, V. O. Golub, E. V. Tartakovskaya, A. V. Chumak, A. A. Serga, B. Hillebrands, and K. Y. Guslienko, Probing dynamical magnetization pinning in circular dots as a function of the external magnetic field orientation, Phys. Rev. B **86**, 054419 (2012).

[35] S. A. Bunyaev, V. O. Golub, O. Y. Salyuk, E. V. Tartakovskaya, N. M. Santos, A. A. Timopheev, N. A. Sobolev, A. A. Serga, A. V. Chumak, B. Hillebrands, and G. N. Kakazei, Splitting of standing spin-wave modes in circular submicron ferromagnetic dot under axial symmetry violation, Sci. Rep. **5**, 18480 (2015).

[36] O. Klein, G. de Loubens, V. V. Naletov, F. Boust, T. Guillet, H. Hurdequint, A. Leksikov, A. N. Slavin, V. S. Tiberkevich, and N. Vukadinovic, Ferromagnetic resonance force spectroscopy of individual submicron-size samples, Phys. Rev. B **78**, 144410 (2008).

[37] E. V. Tartakovskaya, M. Pardavi-Horvath, and R. D. McMichael, Spin-wave localization in tangentially magnetized films, Phys. Rev. B **93**, 214436 (2016).

[38] J. Kharlan, P. Bondarenko, M. Krawczyk, O. Salyuk, E. Tartakovskaya, A. Trzaskowska, and V. Golub, Standing spin waves in perpendicularly magnetized triangular dots, Phys. Rev. B **100**, 184416 (2019).

[39] B. A. Kalinikos and A. N. Slavin, Theory of dipole-exchange spin wave spectrum for ferromagnetic films with mixed exchange boundary conditions, J. Phys. Condens. Matter **19**, 7013 (1986).

[40] A. Vansteenkiste, J. Leliaert, M. Dvornik, M. Helsen, F. Garcia-Sanchez, and B. Van Waeyenberge, The design and verification of MuMax3, AIP Adv. **4**, 107133 (2014).

[41] B. W. Maxfield and W. L. McLean, Superconducting penetration depth of niobium, Phys. Rev. **139**, A1515 (1965).

[42] A. I. Gubin, K. S. Il'in, S. A. Vitusevich, M. Siegel, and N. Klein, Dependence of magnetic penetration depth on the thickness of superconducting Nb thin films, Phys. Rev. B **72**, 064503 (2005).

[43] T. Böttcher, M. Ruhwede, K. Levchenko, Q. Wang, H. Chumak, M. Popov, I. Zavislyak, C. Dubs, O. Surzhenko, B. Hillebrands, A. Chumak, and P. Pirro, Fast long-wavelength exchange spin waves in partially compensated Ga:YIG, Appl. Phys. Lett. **120**, 102401 (2022).
[44] M. Tinkham, *Introduction to Superconductivity* (McGraw-Hill, Inc., New York, 1996).
[45] T. McConville and B. Serin, Ginzburg-Landau parameters of type-II superconductors, Phys. Rev. **140**, A1169 (1965).
[46] S. J. Williamson, Bulk upper critical field of clean type-II superconductors: V and Nb, Phys. Rev. B **2**, 3545 (1970).
[47] https://zenodo.org/records/10405886.
[48] K. Y. Guslienko and A. N. Slavin, Magnetostatic Green's functions for the description of spin waves in finite rectangular magnetic dots and stripes, J. Magn. Magn. Mater. **323**, 2418 (2011).
[49] B. Oripov and S. M. Anlage, Time-dependent Ginzburg-Landau treatment of rf magnetic vortices in superconductors: Vortex semiloops in a spatially nonuniform magnetic field, Phys. Rev. E **101**, 033306 (2020).
[50] T. S. Alstrøm, M. P. Sørensen, N. F. Pedersen, and S. Madsen, Magnetic flux lines in complex geometry type-II superconductors studied by the time dependent Ginzburg-Landau equation, Acta Appl. Math. **115**, 63 (2011).
[51] A. Gulian, *Shortcut to Superconductivity: Superconducting Electronics via COMSOL Modeling* (Springer Nature Switzerland, Cham, 2020).
[52] J. Bardeen, Theory of boundary effects of superconductors, Phys. Rev. **94**, 554 (1954).
[53] A. B. Pippard and W. L. Bragg, Field variation of the superconducting penetration depth, Proc. R. Soc. Lond. A **203**, 210 (1950).
[54] J. E. Sonier, R. F. Kiefl, J. H. Brewer, D. A. Bonn, S. R. Dunsiger, W. N. Hardy, R. Liang, W. A. MacFarlane, T. M. Riseman, D. R. Noakes, and C. E. Stronach, Magnetic field dependence of the London penetration depth in the vortex state of $YBa_2Cu_3O_{6.95}$, Phys. Rev. B **55**, 11789 (1997).